Measuring single-cell density using serial suspended microchannel resonators

by

Max A. Stockslager

B.S. Mechanical Engineering
Georgia Institute of Technology (2015)

Submitted to the Department of Mechanical Engineering
in partial fulfillment of the requirements for the degree of

Master of Science in Mechanical Engineering

at the

MASSACHUSETTS INSTITUTE OF TECHNOLOGY

June 2017

Signature redacted

Author .....
Department of Mechanical Engineering
April 24, 2017

Signature redacted

Certified by .....
Scott R. Manalis
Professor
Thesis Supervisor

Signature redacted

Accepted by .....
Rohan Abeyaratne
Professor
Chairman, Department Committee on Graduate Students

Measuring single-cell density using serial suspended microchannel resonators

by

Max A. Stockslager

Submitted to the Department of Mechanical Engineering

in partial fulfillment of the requirements for the degree of

Master of Science in Mechanical Engineering

Abstract

Cells adjust their composition during important physiological processes, including cell cycle progression, apoptosis, and disease. Due to differences in the densities of water and the various macromolecules which compose cells, changes in cellular composition are reflected by changes in cell density. Previously, methods have been described for measuring density at the single-cell level using suspended microchannel resonators by weighing the same cell in fluids of different densities. Here we describe a high-throughput version of this approach, in which cells are weighed sequentially in three cantilevers containing fluids of different densities. The system design and operation are described, measurement uncertainty is characterized, and single-cell density measurements are compared to those obtained using existing techniques. As a demonstration, we use the system to characterize the biophysical response of $CD8^+$ T cells during activation. We find that single-cell density distinguishes between the phenotypically distinct human $CD8^+$ T cells of healthy vs. chronic lymphocytic leukemia donors, suggesting possible utility as a lymphocyte transformation assay. In summary, the system as described is capable of measuring single-cell density with improved throughput, and the approaches used here for on-chip fluid exchange are applicable to other SMR devices where it is desirable to weigh a cell in multiple fluids, e.g., to measure single-cell growth rate before and after drug or media perturbations.

Thesis supervisor: Scott R. Manalis

Title: Professor

Acknowledgments

I would like to generously thank the many people who have supported me and this research. I am lucky to work with a group of extremely talented people, all of whom make it a pleasure to come into work every morning.

First, thanks to Scott Manalis for the opportunity to work in the lab. Scott has been a fantastic advisor, and I appreciate his constant enthusiasm for trying new things.

Vivian Hecht was a great mentor for the few months that we overlapped in the lab, and I appreciate her taking the time to introduce me to MIT. I enjoyed working closely with Vivian, Josephine Bagnall, and Kevin Hu on the affinity-chip project, and I want to thank Rob Kimmerling for his willingness to share his deep experience with immunology as well as other topics.

I am grateful to Nate Cermak and Selim Olcum for teaching me most of what I know about the SMR, and for their patience in answering my many questions. Nate, in particular, designed the devices used in this thesis and was a huge help in getting them working. Teemu Miettinen and Mark Stevens were always willing to share their perspective as biologists, and have been helpful in trying to identify good research questions to go after. I am thankful to Nick Calistri for sharing his extensive experience with the serial SMR over the course of developing and debugging my various systems. Scott Knudsen has been a great resource for anything science-related. Thanks to all the others in the lab for generally making it a great place to work.

Finally, on a more personal note, I am grateful to my family and to Amy for their constant support through the ups and downs of my being a graduate student.

Contents

List of figures

Chapter 1

Introduction

1.1 Background

1.1.1 Single-cell density as a biophysical parameter

Cells are known to adjust their composition throughout important physiological processes such as cell cycle progression and apoptosis[1], typically resulting in changes in their mass-to-volume ratio. Often, such changes in cell density are used to infer cell state. Perhaps the most common application is density gradient centrifugation, in which mixed populations of cells are separated on the basis of their density. This simple but powerful technique enables, e.g., label-free separation of complex whole blood samples into its components on the basis of the differing densities of erythrocytes (~1.10-1.11 g/mL), vs. lymphocytes (1.072-1.078 g/mL), vs. monocytes (1.06-1.07 g/mL) and other cell types[1,2,3].

Most existing approaches for measuring cell density do so on bulk populations rather than single cells. This is suitable in most applications where density measurements are used in practice, e.g., for separating and collecting large numbers of blood cells of interest from a population. However, recent developments have enabled precise measurement of the density of *single* cells using suspended microchannel resonators (SMRs)[1,4,5]. In some cases, the improved precision of these measurements can be used to identify very subtle shifts in cell state[6,7]. For example, by repeatedly measuring the density of the same cell for the duration of the cell cycle, it has been shown that suspended cells swell with water over a 20-minute period during mitosis, reflected by a decrease in density of order 0.4% (ref. [6]). In another case, single-cell density measurements using the SMR were used to tease apart changes in cell state following nutrient withdrawal from growth-factor-deprived lymphocytes[7]. Taken together, these examples suggest that single-cell density measurements can serve as a useful window into the internal state of the cell, providing information that is often not accessible from other biophysical measurements such as buoyant mass or mass accumulation rate.

In addition to measuring mass, volume, and density, the SMR has also been used to measure the dry mass, dry volume, and dry density of single cells, where "dry" refers to non-aqueous content[8]. Dry mass can also be measured using quantitative phase microscopy[9], with the advantage of being able to measure many cells in a field of view simultaneously. However, precision is limited since QPM measurements require some assumptions regarding the cells' composition, since carbohydrates, proteins, and lipids contribute differently to the refractive index[8].

1.1.2 The suspended microchannel resonator

The suspended microchannel resonator (SMR) is a microfluidic mass sensor used to precisely measure the buoyant mass of single cells in solution. Its design and operation have been described previously[10,11]. Briefly, the sensor consists of a vacuum-packaged cantilever with an embedded fluidic channel. A "chip" containing one or more cantilevers is continually vibrated at its resonance frequency using a piezoelectric actuator, and the resulting deflection of each cantilever is measured using either an optical lever or embedded piezoresistive sensors. As a cell flows through the fluidic channel and enters a cantilever, if the cell's density differs from that of the surrounding fluid, the cantilever's total mass changes, resulting in a change in the cantilever's resonance frequency. The core idea of resonant mass sensors is that by measuring the magnitude of the frequency shift, we can estimate the mass of the cantilever (and in this case, the mass of the cell and fluid within the embedded fluidic channel). The maximum shift in resonance frequency is proportional to the cell's *buoyant mass*, i.e., the mass of the cell minus the mass of the fluid it displaces.

Several approaches exist for precisely measuring such shifts in resonance frequency. In principle, a change in resonance frequency could be detected in open-loop, e.g., by sweeping the drive signal across a range of frequencies and measuring the resulting amplitude of the deflection signal; the resonance frequency is the frequency at which the amplitude of the deflection signal is maximized. However, this approach lacks the required bandwidth for real-time tracking of the transient resonance frequency changes that occur due to cell or particle transit through a cantilever, where typical transit times are of order 0.1-0.5 s.

An alternative approach to tracking resonance frequency is to drive the cantilever at a fixed frequency and measure the time-varying phase shift between the drive signal and the measured amplitude signal. This approach allows for greater measurement bandwidths, but suffers from lower dynamic range, particularly in the case of high quality factors. The problem of limited dynamic range can be solved using a phase-locked loop, which uses this phase shift measurement to adjust the drive frequency such that the drive signal continuously tracks the cantilever's resonance frequency, maintaining a phase shift of 90° between the input and output signals[12]. As described previously in the context of the SMR, this approach achieves measurement bandwidths as high as 500 Hz[12].

1.1.3 Measuring single-cell density using the SMR

The suspended microchannel resonator measures a cell's buoyant mass, which is a function not only of cell size but also of the properties of the fluid. A cell's buoyant mass in a particular fluid is related to its volume, density, and absolute mass by Eq. (1),

$$m_b = m_{cell} - \rho_f V_{cell} = (\rho_{cell} - \rho_f) V_{cell} \tag{1}$$

where m_b is the cell's buoyant mass, m_{cell} is the cell's absolute mass, ρ_{cell} is the cell's density, ρ_f is the fluid density, and V_{cell} is the cell's volume. As described previously[1,4,8], weighing a cell in two fluids of different densities allows us to solve for its *absolute* mass, volume, and density. To see this, we can express the two buoyant mass measurements as

$$\begin{bmatrix} m_b^1 \\ m_b^2 \end{bmatrix} = \begin{bmatrix} 1 & \rho_f^1 \\ 1 & \rho_f^2 \end{bmatrix} \begin{bmatrix} m_{cell} \\ V_{cell} \end{bmatrix} \tag{2}$$

If the fluid densities are different, the fluid density matrix is invertible and we can write

$$\begin{bmatrix} m_{cell} \\ V_{cell} \end{bmatrix} = \frac{1}{\rho_f^2 - \rho_f^1} \begin{bmatrix} \rho_f^2 & -\rho_f^1 \\ 1 & -1 \end{bmatrix} \begin{bmatrix} m_b^1 \\ m_b^2 \end{bmatrix} \tag{3}$$

where the cell's density is the ratio m_{cell}/V_{cell}. This approach has a convenient geometric interpretation: when the buoyant mass measurements are plotted against fluid density and a line is fit to the measurements, the (negative) slope of the resulting line is the cell's volume, the *y*-intercept is the cell's absolute mass, and the *x*-intercept is the cell's density (Fig. 1). This is most clear from consideration of Eq. 1.

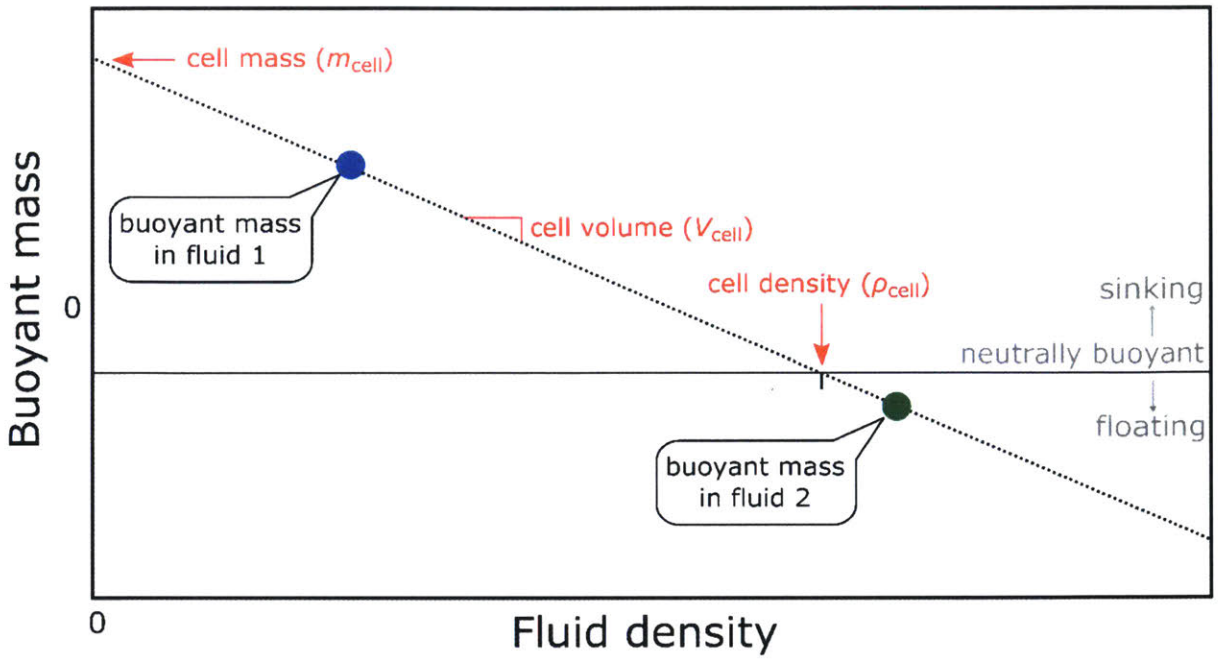

Figure 1. A cell's mass, volume, and density can be determined from two measurements of the cell's buoyant mass in fluids of different densities.

Several approaches have been developed previously to measure a cell's buoyant mass in two different fluids using the SMR[1,4,13,5] . One such approach is depicted in Fig. 2. A cell enters the device through the left bypass channel in the first (red) fluid. The cell flows through the cantilever and its buoyant mass is measured, then it enters a second bypass channel filled with the second (blue) fluid. The direction of flow is then reversed, and the cell passes back through the cantilever as its buoyant mass is measured in the second fluid. The first bypass is then flushed with the first fluid, and the process is repeated for the next cell. After the measurement is completed, the buoyant mass measurements corresponding to the same cell are matched and each cell's mass, volume, and density are computed.

The achievable throughput of this approach is limited by the time required to allow the two fluids to mix via diffusion; in some cases, this can be as long as 15 sec [ref. 4]. A more practical limitation of this approach is that the system often requires fine tweaking of the fluid control settings to balance the requirements of achieving good fluid mixing while still ensuring that every cell returns to the cantilever to be measured in the second fluid.

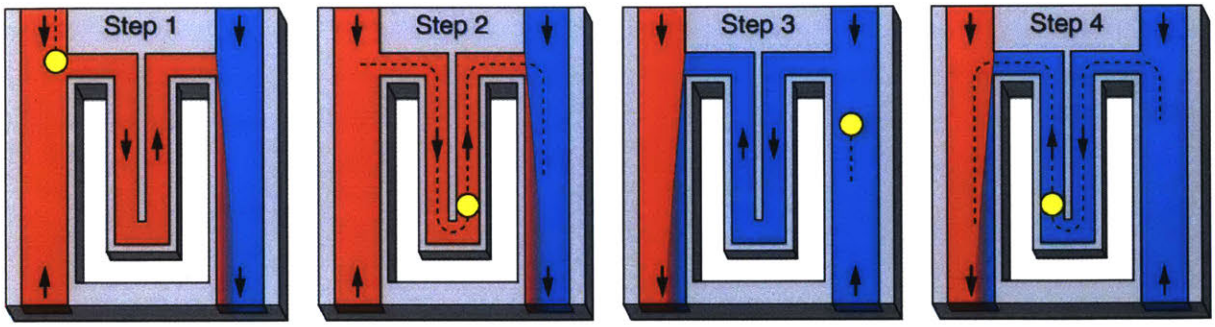

Figure 2. Single-cantilever approach to measuring the density of single cells. Adapted from ref. [1].

An alternative approach was developed to measure single-cell density with improved throughput compared to the fluid-exchange approach. To avoid the need to exchange the fluid within the cantilever (which requires waiting for the fluids to mix), the "dual SMR" incorporated two sensors on the same chip, one dedicating to weighing each cell in each of the two fluids (Fig. 3)[4]. A cell enters the device from the sample bypass and its buoyant mass is measured in the first sensor (SMR_1) in the low-density fluid (typically media). Next, the cell flows through a cross-junction where most of the surrounding fluid is exchanged for a higher-density fluid. The cell flows through a serpentine delay channel to allow time for the low- and high-density fluids to mix, then its buoyant mass is measured in a second sensor. Similar to the fluid-exchange approach, the buoyant mass measurements in each sensor that correspond to the same cell are paired, and each cell's mass, volume, and density are computed from each pair of measurements.

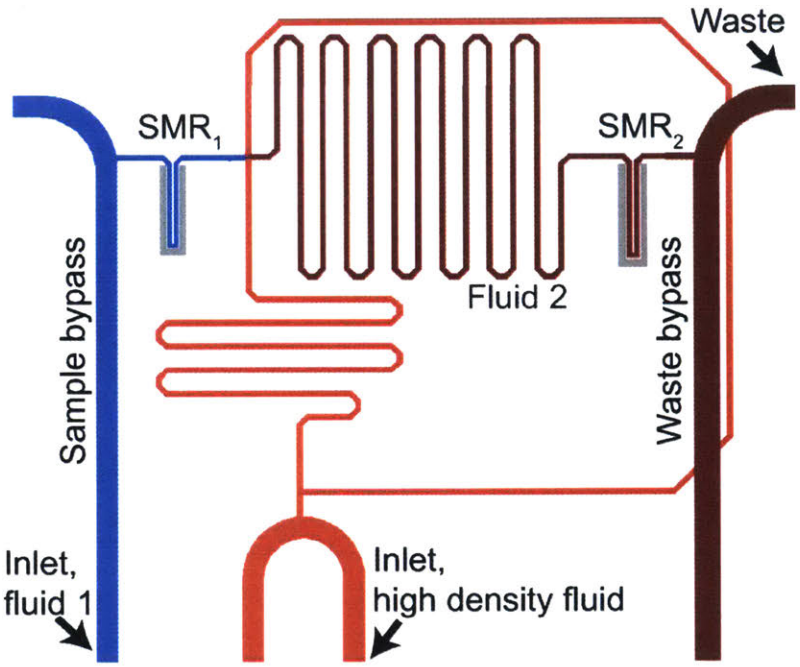

Figure 3. Fluidic design of the dual SMR, used for weighing single cells in two fluids. Adapted from ref. [4].

Two factors provide upper bounds on the throughput of the dual SMR. One limiting factor is related to data analysis downstream of the measurement. At very high cell concentrations, it is difficult to determine which "peaks" in the two resonance frequency signals correspond to the same cell. In practice this limits the rate that cells can enter the device to (at most) several times shorter than the delay time between the sensors.

A second limitation on throughput – which ends up being the dominant limitation for the dual SMR – is related to the stability of the resonance frequency signal in the second cantilever in response to small changes of fluid density. It was observed that as cells flow past the cross-junction where fluid exchange occurs, they perturb their flow in such a way that their local fluid density is slightly different from that of the bulk fluid[14]. This is a problem because a typical SMR has responsivity of order 1 MHz/(g/mL), so transient fluid density changes as small as 10 ppm can obscure the resonance frequency shifts corresponding to a cell. Fig. 4 plots two examples of first-mode peaks observed in the second cantilever of the dual SMR.

Since these transient changes in fluid density typically occur when cells pass through the cross-junction, in practice they could be mitigated by using lower cell concentrations; with fewer cells in the device, upstream changes in fluid density were less likely to propagate downstream to

the second cantilever while a cell was being measured. Given these two upper bounds, the dual SMR was able to achieve throughputs of approximately 5 cells min^{-1} (ref. [4]).

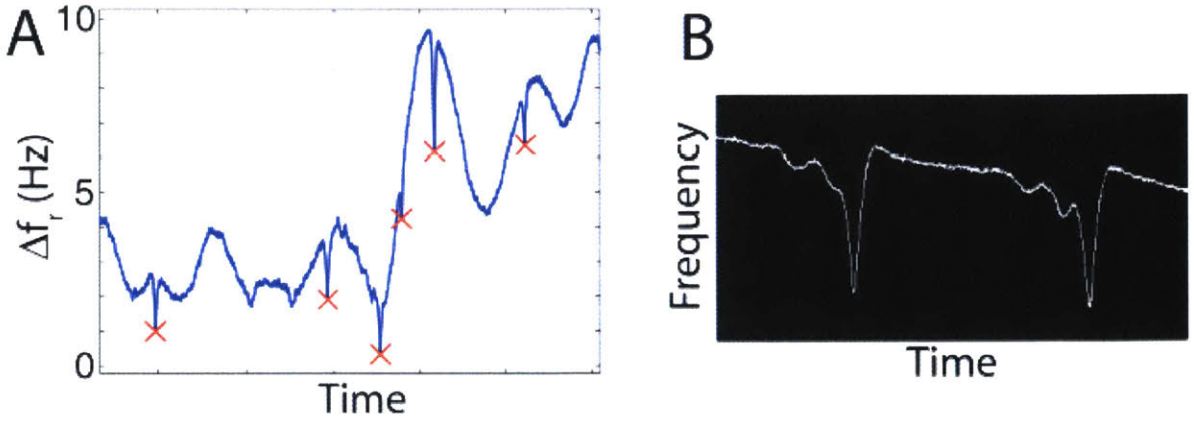

Figure 4. Transient fluid density changes can obscure frequency shifts corresponding to cells in the dual SMR. Adapted from ref. [14].

1.2 Objectives

This thesis describes the development of a three-cantilever SMR device for measuring the buoyant mass of a single cell sequentially in three different fluids. Unique features of the system's design and operation are described, as well as key features of the methods used for data analysis. Measurement uncertainty is characterized, and performance is compared to existing techniques for measuring single-cell density. As a demonstration, the system is used to characterize the biophysical changes occurring during T cell activation in both murine and human model systems. Finally, I discuss the possibility of using the device to simultaneously measure the density and dry density of single cells.

The approaches developed in this thesis, e.g., for on-chip fluidic exchange, are applicable to other SMR device designs in which it is desirable to weigh a cell in multiple fluids, e.g., to measure single-cell mass accumulation rate before and after drug or media perturbations.

Chapter 2

System design and development

2.1 Three-cantilever device

Fig. 5 shows a schematic of the three-cantilever fluid-exchange device. A cell enters the array in a low-density fluid through the left bypass. Next, it enters the first buried channel and is measured in the first sensor. The cell then enters a long mixing channel containing the high-density fluid, where it spends approximately five seconds before entering the second buried channel and the second sensor. The cell then enters a second mixing channel where the medium is exchanged for the low-density fluid before being measured for a third time in the last sensor.

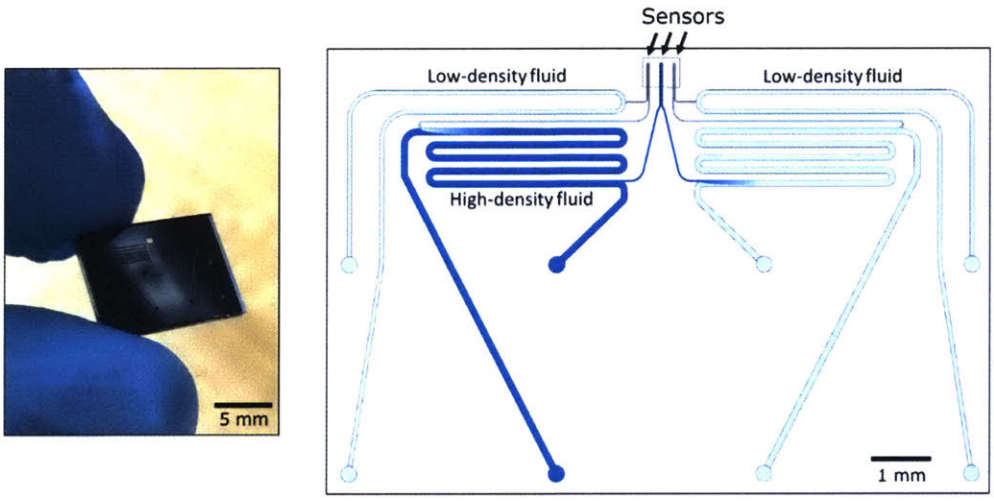

Figure 5. Three-cantilever device for measuring single-cell density.

There are several key differences between the three-cantilever device and the dual SMR. The first and most obvious difference is the inclusion of a third cantilever. This third buoyant mass measurement can serve one of two functions: either (1) improve the precision of our density estimate by weighing the cell in *three* fluids of different densities, or (2) weigh the cell in a third fluid to which the membrane is permeable, potentially enabling simultaneously measurement of a cell's density *and* dry density. (Appendix 1 discusses this possibility).

A second important difference between the three-cantilever device and the dual SMR is the design of the fluid exchange channel, intended to enhance fluid mixing and mitigate the stability problems described previously. Apart from geometry changes (this mixing channel is wider than that of the dual SMR; 150 μm, vs. 25-100 μm), the two devices differ in the branching structure of their fluidic channels. As shown in Fig. 3, in the dual SMR, the second cantilever is in *series* with the mixing channel, i.e., all fluid entering the mixing channel will go on to pass through the second cantilever. But in the three-cantilever device (Fig. 5), only a small fraction of the fluid in the mixing channels enters the following cantilevers, while the rest of the fluid in the mixing channel flows *past* the entrance to the lead channels and is flushed out of the chip. It is possible to allow only a small amount of flow into the lead channels from the mixing channels – and if the flow is controlled appropriately, all cells will travel on streamlines which *do* pass through all three cantilevers.

As described in Section 3.4, it appears that the combination of these two changes from the dual SMR resulted in improved fluid mixing and baseline stability.

2.2 Readout, imaging, and environmental control

With slight modifications, the system used to read out the three cantilevers' resonance frequencies is similar to systems described previously[12,15].

Deflection of the cantilevers is read out using an optical lever setup. The three cantilevers are illuminated simultaneously using a superluminescent diode (Superlum, Ireland), focused into a line on the tips of the cantilevers. The laser is focused into a line using collimating asphere and a cylindrical lens, then recollimated using a convex doublet. The beam passes through a polarizing beam splitter and quarter wave plate, before being refocused onto the cantilevers using a second convex doublet. A pair of mirrors is used for alignment of the laser beam relative to the optical system, and a two-axis stage is used to align the cantilevers relative to the laser.

After reflecting off the cantilevers, the deflected beam passes back through the quarter-wave plate and is reflected by the polarizing beam splitter through a focusing cylindrical lens and onto a split photodiode. The difference between the two photodiode channels is amplified and read by a field programmable gate array (Altera DE2-115) for further processing. The photodetector signal reflects a superposition of the deflections of the three cantilevers.

We considered using a Mylar pinhole array at the focal plane of the cylindrical lens so that three distinct spots rather than a single beam would be focused on the cantilevers. This would reduce the amount of light reflecting back to the photodetector off of the glass packaging rather than the cantilevers, potentially increasing the signal-to-noise ratio in the photodetector signal. However, in practice, we found that lower noise was achieved without the pinhole array; despite the reduction in background noise, the pinhole array also resulted in much less light reaching the cantilevers, resulting in lower-amplitude photodetector signals.

The temperature of the chip and sample vials were maintained at 37°C using a recirculating water bath (NESLAB RTE-111). Fluidic connections to the device were made using perfluoroelastomer O-rings, which were preloaded between the device and an aluminum face plate to form a seal. For monitoring cell loading, the device was imaged using an upright microscope (Nikon) with a 4x objective (Nikon), and video was recorded at 15 frames per second using an Edmund Optics 1312C camera. Due to the relatively short measurement duration, sample and buffer vials were pressurized with filtered house air rather than CO_2, which did not appear to negatively affect cell viability.

2.3 Fluidic control

2.3.1 Hardware

Pressure-driven flow through the device was controlled by eight electronically-controlled pressure regulators (ProportionAir), which pressurized sealed Wheaton vials. One pressurized sample vial was connected to the upstream and downstream ends of each of the four bypasses channels (vertical branches in Fig. 6).

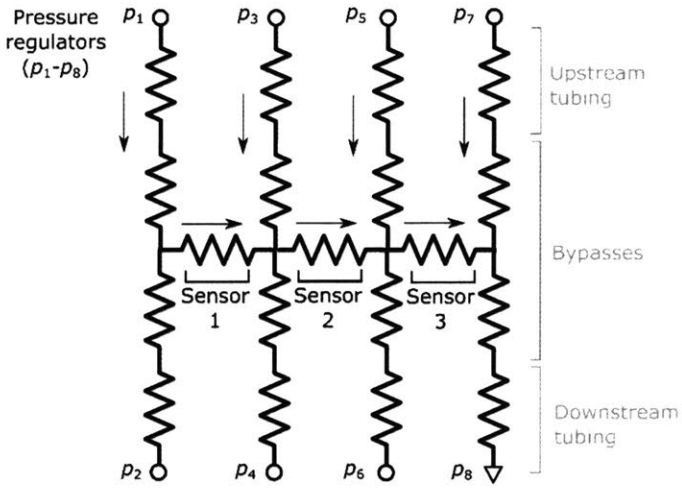

Figure 6. Resistive network model for flow through the three-cantilever device. Pressure is controlled at the eight external nodes to control flow across each of the eleven branches of the network.

2.3.2 Fluidic network model

A key design requirement is independent control of the pressure difference (and therefore flow rate) *along* each of the four bypasses and *across* each of the three sensors. To set these pressure at each of the regulators, we need a model to relate the pressures applied by the regulators at the external nodes to the resulting *flow* across each branch of the fluidic network. To relate applied pressures to flow through the network, we use the known channel and tubing dimensions to estimate the resistances in Fig. 6 from the standard solution for unidirectional viscous flow: $R \stackrel{\text{def}}{=} \Delta P/Q = 128\mu L/\pi D^4$, where for non-circular channels we define the "hydraulic diameter" $D = 4A/P$ where A is the channel's cross-sectional area and P is its perimeter.

Once these resistances are known, we can write a set of linear equations (enforcing conservation of mass at each node of the network) relating flow through each branch of the fluidic network to the pressures applied at the external nodes, then solve this system to compute the external pressures required to generate specified flow rates throughout each branch of the device. Appendix 2 describes this general approach in detail, which can be modified for any device geometry.

For this particular device design, we can make some simplifications to spare us from having to use the full machinery described in Appendix 1. For this device geometry, we can approximate

the pressure at each internal node as the average of the pressures in the adjacent external nodes, e.g., $p_9 \approx (p_1 + p_2)/2$. This approximation is reasonable if we assume that (1) the total fluidic resistance of each bypass-channel-plus-tubing branch is approximately equal, and (2) the resistance of the buried channel leading to each cantilever is much larger than the resistances of the bypass channels. For this device geometry, these assumptions are reasonable; in particular, to satisfy (1), we chose to use relatively small i.d. tubing (0.003", or 76 μm) to introduce fluids to the device so that any minor differences in bypass geometry would be dominated by the large resistance of the tubing.

Given these assumptions, the pressure difference along each edge of the network (bypasses 1-4, cantilevers 1-3) can be computed from the pressures applied by the regulators by describing the channel layout using a weighted incidence matrix A:

$$\Delta P \stackrel{\text{def}}{=} \begin{pmatrix} \Delta p_{B1} \\ \Delta p_{B2} \\ \Delta p_{B3} \\ \Delta p_{B4} \\ \Delta p_{C1} \\ \Delta p_{C2} \\ \Delta p_{C3} \end{pmatrix} = \begin{pmatrix} 1 & -1 & 0 & 0 & 0 & 0 & 0 \\ 0 & 0 & 1 & -1 & 0 & 0 & 0 \\ 0 & 0 & 0 & 0 & 1 & -1 & 0 \\ 0 & 0 & 0 & 0 & 0 & 0 & 1 \\ 1/2 & 1/2 & -1/2 & 0 & 0 & 0 & 0 \\ 0 & 0 & 1/2 & 1/2 & -1/2 & -1/2 & 0 \\ 0 & 0 & 0 & 0 & 1/2 & 1/2 & -1/2 \end{pmatrix} \begin{pmatrix} p_1 \\ p_2 \\ p_3 \\ p_4 \\ p_5 \\ p_6 \\ p_7 \end{pmatrix} \stackrel{\text{def}}{=} AP$$

Here, the pressure downstream of the fourth bypass is taken as the "ground" or reference pressure ($p_8 \stackrel{\text{def}}{=} 0$), so we have seven degrees of freedom to control the pressure differences across the four bypasses and three cantilevers. Since the incidence matrix A is invertible, for any desired combination of pressure differences ΔP we can compute the required external pressures P. This approach can be modified for any device design by modifying A to reflect the layout of the fluidic network, including approximate fluidic resistances if the simplifying assumptions above don't hold. However, it is important to note that while there exists a unique pressure vector P that gives any desired combination of pressure differences, we may still be limited by hardware; for example, the ProportionAir regulators used here are limited to 0-30 psi (i.e., cannot apply negative/vacuum pressures).

In summary: when operating the device, we specify a pressure difference or (equivalent) flow rate that we want across each branch of the fluidic network, then use the computations described above to appropriately set the pressure regulators to achieve these pressure differences or flows.

Chapter 3

Analysis

3.1 Peak matching

In any SMR system where single cells are weighed multiple times in different sensors, it is necessary to identify which peaks in each of the sensors' resonance frequency signals correspond to the same cell. The approach used to accomplish this depends on the nature of the measurement. Typically, the task is nontrivial because (1) some cells fail to pass through all three sensors, and (2) the peaks corresponding to some cells may not be detected by the analysis software, e.g., because two cells might enter a sensor at the same time and be detected as a single buoyant mass. Developing an efficient procedure for matching cells is key, because in some cases it is the dominant factor limiting the total throughput of the system.

The data analysis pipeline for the dual SMR used the Needleman-Wunsch algorithm to accomplish a similar "matching" task. The algorithm comes from bioinformatics, where it is typically used to align nucleotide sequences. Peaks are matched based on the expected time between sensors, with the option to assign peaks to a "gap" if a cell appears not to have passed through both sensors. However, this approach does not account for the possibility of one cell passing another as they travel between sensors. In practice, this requires lower cell concentrations and limiting throughput to obtain reliable matching.

An alternative approach was developed previously to match buoyant mass measurements in a serial SMR array to measure single-cell growth rates[15]. This approach uses prior estimates of growth rate and transit time between sensors to estimate the likelihood that any two peaks in different sensors correspond to the same cell, i.e., the algorithm matches buoyant mass measurements from different sensors in such a way that our prior estimates of growth rate and transit time through the device are minimally violated. A modified version of this approach was implemented here, with our "prior expectations" specified in terms of density rather than growth rate.

Briefly, the matching algorithm works as follows. We first assemble a list of the buoyant masses measured in each sensor and the time at which they occurred. We then compare each of

the n_1 peaks in the first sensor with each of the n_2 peaks in the sensor, and assign a cost to each of these $n_1 n_2$ postulated matches, given our prior estimates of transit time and cell density (for example, most cells pass through the second sensor 4-6 seconds after they pass through the first sensor, so two peaks separated in the first second sensors by 30 seconds are an unlikely match and would be assigned a high cost). The process then is repeated to assign costs to the $n_2 n_3$ possible pairings between the measurements in the second and third cantilevers. We then find the optimal assignment which minimizes these two matrices of costs, using a method called the Hungarian algorithm (also known as Munkres' algorithm)[16]. A provision is included to not match a cell if it seems unlikely to correspond to any of the peaks detected in the other two sensors.

The key to this approach is assigning an appropriate cost to a postulated pair of cells to be matched. A cost is assigned to a pair of buoyant mass measurements as follows. Given two buoyant mass measurements $m_{b,1}$ and $m_{b,2}$ observed in sensors with fluid densities ρ_1 and ρ_2 at times $t_1$and t_2 respectively, we compute the transit time $\Delta t = t_2 - t_1$ and the implied cell density $\rho_{cell} = (\rho_2 m_{b,1} - \rho_1 m_{b,2})/(m_{b,1} - m_{b,2})$. Given prior estimates on cell density and transit time (for example, $\mu_\rho \stackrel{\text{def}}{=} 1.05$ g/mL, $\mu_{\Delta t} \stackrel{\text{def}}{=} 5$ sec), we define the cost of matching the two cells as

$$\text{Cost} = -\ln\left[\mathcal{N}\left(\rho_{cell};\, \mu_\rho, \sigma_\rho^2\right)\right] - \ln[\mathcal{N}(\rho_{\Delta t};\, \mu_{\Delta t}, \sigma_{\Delta t}^2)]$$

where $\mathcal{N}(x;\, \mu, \sigma^2)$ indicates the normal probability density function with mean μ and variance σ^2 evaluated at x.

Fig. x plot contours of constant cost for a representative cell (40 pg buoyant mass in fluid 1), given fluid densities of 1.00 g/mL, 1.04 g/mL, and 1.02 g/mL in the first, second, and third sensors respectively. We expect to observe peaks near the center of each "ring" in buoyant mass-time space, and penalize any peak observations further away from the center as unlikely matches. The matching algorithm penalizes buoyant mass deviations from the expected value more greatly in the third sensor since (in this case) its density is closer to the density of the first fluid; when two sensors have more similar fluid densities, small shifts in buoyant mass correspond to greater

changes in implied cell density.

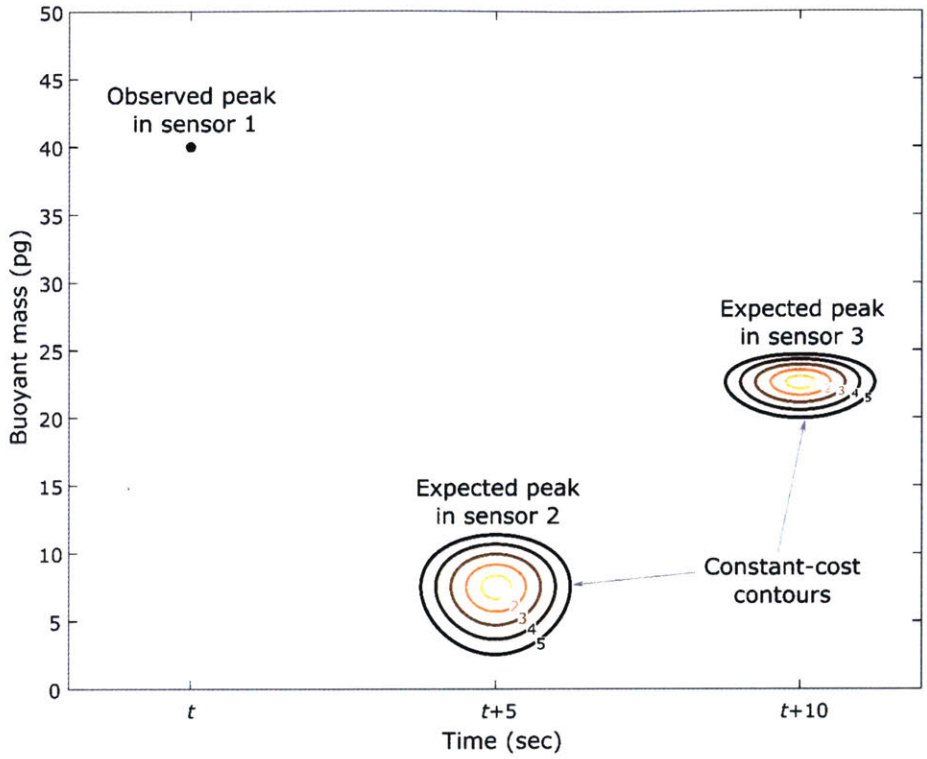

Figure 7. Contours of constant matching cost, given a 40 pg buoyant mass observed in the first sensor at time t, with fluid densities of 1.00 g/mL, 1.04 g/mL, and 1.02 g/mL in the first, second, and third sensors respectively. The expected transit time between sensors is 5 sec and the expected cell density is 1.05 g/mL. Cells further from the expected time and buoyant mass are assigned higher costs.

The human eye is generally good at performing this type of matching task, so it is easy to confirm whether the matching algorithm did a good job. Fig. 8 plots the resonance frequency signals in the three sensors for a representative measurement. Peaks corresponding to the same cell are indicated with the same color in the three sensors. In this example, cells were separated by an average of ~7 seconds, but the closest-spaced cells were separated by as little as 1-2 seconds, and generally the matching was still successful. In general, good matching is possible for measurement throughputs *averaging* as high as 5-10 cells min^{-1}. After matching, each three-cell match was manually approved or rejected, and matching parameters (e.g. expected transit time or expected density) were adjusted if necessary.

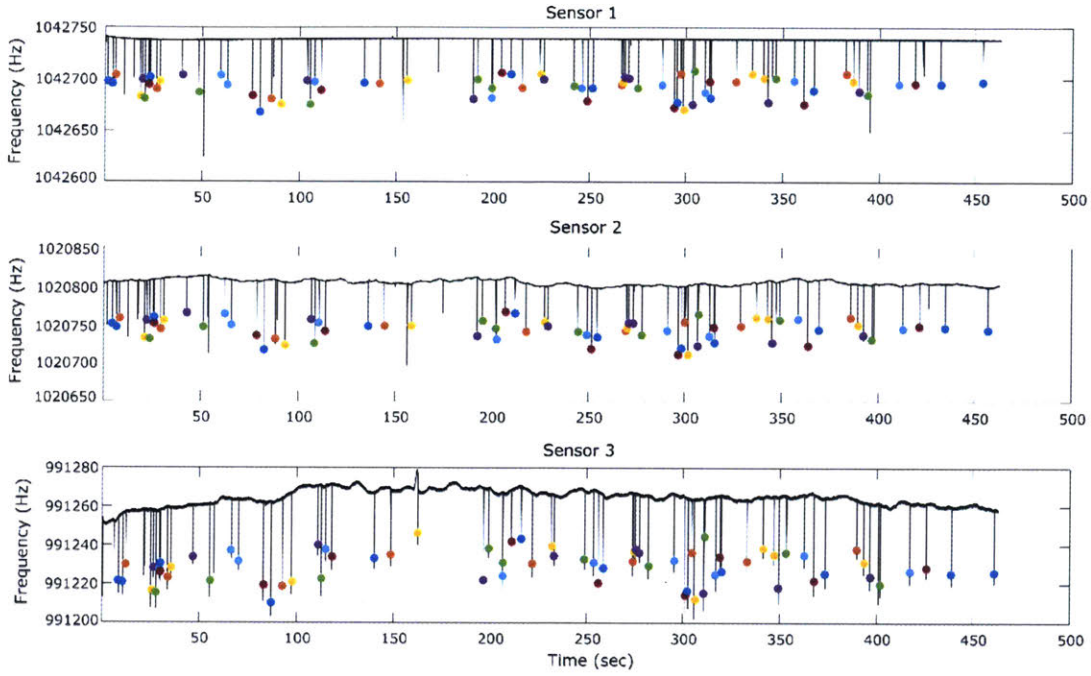

Figure 8. Sample density measurement, with matches overlaid on peaks as colored circles, with the same color corresponding to the same cell in all three sensors. Sixty-eight cells were measured in eight minutes, average seven seconds average separation between cells.

It is worth noting that the distribution of times between cells entering the array is approximately exponential, or memoryless. When the *mean* spacing between cells is T, the *distribution* of times between cells entering the array is[17]

$$P(t|T) = (1/T)e^{-t/T}$$

Accurate matching is a function of the *minimum* spacing between cells, while throughput is a function of the *mean* spacing between cells. To ensure that at least a fraction f of cells entering the device are separated by at least a minimum time spacing t_{min}, the mean spacing between cells must be at least

$$T_{avg} > \frac{t_{min}}{\ln(1/f)}$$

which constrains the average throughput of cells through the device. For example, if we require that $f = 90\%$ of cells entering the device are separated by $t_{min} = 1$ sec, then the average throughput is constrained to $T_{avg} > 9.5$ sec. This value increases rapidly as f approaches 1; for example, when $f = 99\%$, the average spacing must exceed the desired minimum spacing by ~100

fold. This highlights the need for "active loading" techniques to better control the loading of cells into the array.

3.2 Density calculation

We can take advantage of the third cantilever to improve the precision of our estimate of the cell's density. In general, if we have weighed a cell multiple times, making n buoyant mass measurements $m_b^1 \ldots m_b^n$ in fluids of density $\rho_f^1 \ldots \rho_f^n$, we estimate the cell's absolute mass and volume by solving the linear system

$$M_b = \begin{bmatrix} m_b^1 \\ \vdots \\ m_b^n \end{bmatrix} = \begin{bmatrix} 1 & \rho_f^1 \\ \vdots & \vdots \\ 1 & \rho_f^n \end{bmatrix} \begin{bmatrix} m_{cell} \\ V_{cell} \end{bmatrix} = A \begin{bmatrix} m_{cell} \\ V_{cell} \end{bmatrix}$$

As described previously, for $n = 2$, A is invertible and we can solve for the cell's mass and volume:

$$\begin{bmatrix} m_{cell} \\ V_{cell} \end{bmatrix} = \frac{1}{\rho_f^2 - \rho_f^1} \begin{bmatrix} \rho_f^2 & -\rho_f^1 \\ 1 & -1 \end{bmatrix} \begin{bmatrix} m_b^1 \\ m_b^2 \end{bmatrix}$$

from which the cell density is computed as the ratio m_{cell}/V_{cell}. However, for $n > 2$, A becomes singular and the problem is overconstrained; it's not possible to find an *exact* cell density that is consistent with the three observed buoyant masses and fluid densities. Instead, the least squares solution can computed from the buoyant mass measurements as $\begin{bmatrix} m_{cell} \\ V_{cell} \end{bmatrix} = (A^T A)^{-1} A^T M_b$; we are effectively choosing the values of cell mass and volume that best explain the buoyant mass observations we have observed. This has the same convenient geometric interpretation shown in Figure 1, except now we are using the slope and intercepts of the *best-fit line* to compute the cell's mass, volume, and density.

3.3 Measurement uncertainty

We now turn to estimating the improvement in density measurement precision that is obtained by including a third buoyant mass measurement. Since cell density is a nonlinear function of the three buoyant mass measurements, we used Monto Carlo simulations, as described previously in the context of dry density measurements[8].

To simulate measurement error, we fix the mass and density of a hypothetical cell, then compute its true buoyant mass in each of three fluids (densities 1.00 g/mL, 1.02 g/mL, and 1.04

g/mL). Known measurement error is added to each of the buoyant masses (sampled from a normal distribution with $\mu = 0$ pg, $\sigma = 0.1$ pg), then density is re-computed. The process is repeated thousands of times to assess the distribution of the resulting density estimates. Fig. 9 plots the 95% confidence interval on the resulting density estimate, for a cell with a true density of 1.05 g/mL. Including the third buoyant mass measurement in the density estimate substantially decreases measurement uncertainty (solid versus dot-dashed lines).

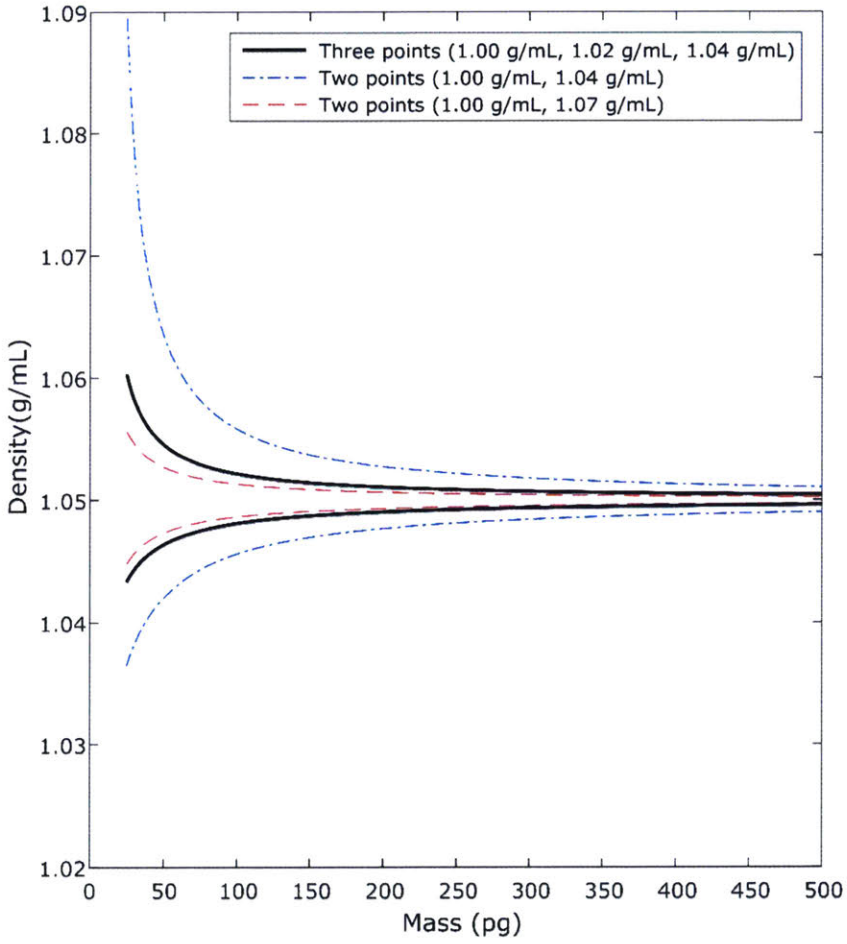

Figure 9. 95% confidence bounds on density measurement for a cell of fixed density. The uncertainty depends on the cell mass (represented on the *x*-axis) and the fluid densities used to make the measurement (legend).

Measurement uncertainty also varies significantly with fluid density. For a cell with density 1.05 g/mL, having two buoyant mass measurements taken in fluids of density 1.00 g/mL and 1.07

g/mL (typical for the fluid-switching method), density uncertainty is slightly better than the three-cantilever density measurement, particularly for small cells (150 pg; Fig. 9). However, the performance is nearly identical for the sizes of cells typically measured in practice. This occurs because measurement uncertainty is improved when one fluid is more dense than the cell and the other is less dense than the cell. This is discussed more fully in the supplementary information of ref. [8]. Future work on the three-cantilever device may include modifying the fluidics to obtain a measurement in a high-density fluid to improve the precision of the density measurements.

3.4 Baseline stability

As discussed previously, one key limitation of the dual SMR was instability in the baseline resonance frequency resulting from transient changes in fluid density (Fig. 4). As designed, the three-cantilever devices do not suffer from baseline instability to the same degree (Fig. 9).

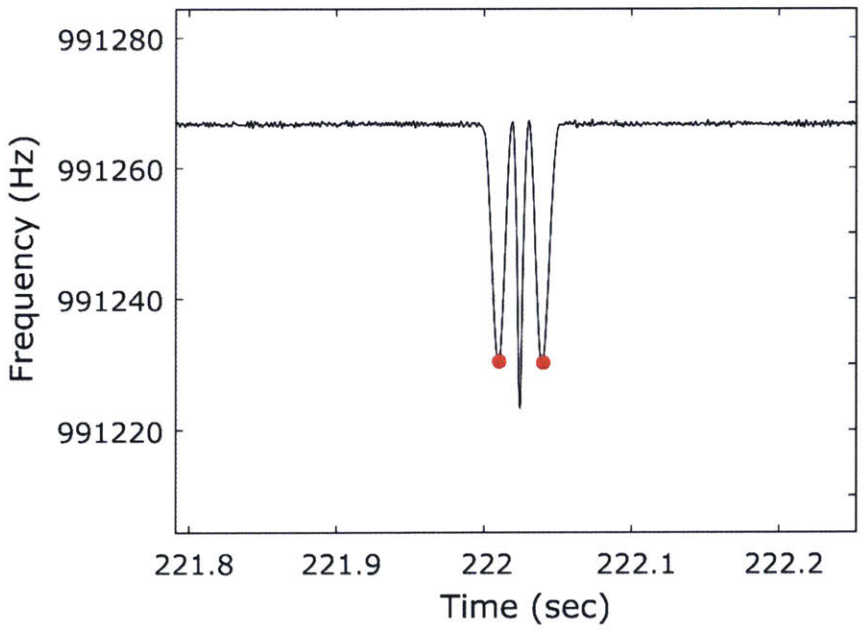

Figure 10. Typical second-mode peak in the three-cantilever device, showing improved baseline stability.

While it is not exactly clear which features of the new devices have led to this improved performance, there are several possibilities. First, fluid mixing may be more uniform due to the

design of the mixing channels in this device. The key difference in geometry is increased width in the mixing channel (150 μm, vs. 25-100 μm in the dual SMR).

But why would increased mixing channel width lead to more uniform mixing? One potential benefit is that at low Reynolds number, the effective dispersivity in the direction of the flow increases with the channel width, a phenomenon called Taylor dispersion. Rewriting the continuity equation in terms of cross-sectional average velocity and species concentration results in an expression for an "effective dispersivity" D_{eff} which is a function of the channel-width Peclet number Pe_d (ref [18]):

$$\frac{\partial \bar{c}}{\partial t} + \bar{v}\frac{\partial \bar{c}}{\partial z} = D\left(1 + \frac{1}{192}Pe_d^2\right)\frac{\partial \bar{c}}{\partial z} = D_{eff}\frac{\partial \bar{c}}{\partial z}$$

where $\bar{c}$ is the cross-sectional average species concentration, $\bar{v}$ is the cross-sectional average velocity, and $Pe_d = d\bar{v}/D$. Due to the increased channel width, dispersion is enhanced in the longitudinal direction by a factor of $\left(1 + \frac{1}{192}Pe_d^2\right)$. This enhanced dispersion acts to smooth out longitudinal fluctuations in fluid density, and (in this case) reduce variations in the cantilever's baseline resonance frequency.

A second, more practical method of mitigating baseline instability is to simply flow cells through the device faster. Since fluctuations in baseline fluid density typically happen over time scales of seconds, flowing cells through each sensor with transit times of 50-100 ms allowed rejection of baseline variation when each peak was analyzed, allowing us to accurately recover the buoyant mass of each cell. Resolving these rapid frequency changes required increased PLL bandwidth (200-300 Hz increased from typically 100 Hz), sacrificing some high-frequency noise rejection in exchange for increased baseline stability in the neighborhood of each peak. Apart from bandwidth, the main concern with increasing flow rates is the increased shear stress on cells (which scales proportional to V). However, for the flow rates typically used, excessive shear stress did not appear to be a problem since measuring the density of some common cell lines (e.g., L1210) yielded measurements similar to those obtained using both single-cantilever devices and the dual SMR[1,4].

Chapter 4

Applications of high-throughput single-cell density measurements

4.1 T cell activation

Upon engagement of the T cell receptor by its cognate antigen, T cells begin to rapidly grow and proliferate in order to build up a population of antigen-specific cells to initiate the immune response. In some instances, this extent of this proliferative response is used as a measure of the relative strength of the T cells' response to antigen stimulation. In these assays, T cell proliferation is typically measured via ^{3}H-thymidine uptake[19], or size can by approximately measured from forward light scatter[20].

We wondered whether precise single-cell mass, volume, and density measurements could be useful as a rapid indicator of the extent of T cell activation. We used murine $CD8^{+}$ T cells isolated from a healthy mouse, and human $CD8^{+}$ T cells derived from both healthy and CLL (chronic lymphocytic leukemia) blood samples.

4.1.1 Murine CD8+ T cells

We isolated $CD8^{+}$ T cells from the spleen of a wild-type mouse using techniques described previously (see Materials and Methods for details). The T cells were activated by stimulation with anti-mouse CD3 with co-stimulation from anti-mouse CD28, with mouse IL-2 and beta-mercaptoethanol in solution. The population was sampled and density was measured at six time points spread across the first 48 hours of activation (Fig. 11). As soon as 8 hours after activation, a clear subpopulation of cells has begun to increase in volume and decrease in density. This fraction of cells continues to grow in number – increasing in mass and decreasing in density – until the final time point, where approximately 69% of cells have departed from the mass and density of the naïve population, measured via gating. The median cell mass decreased at some point between 32 and 48 hours, perhaps indicating that the largest cells had finally undergone their first division and no new cells reached these sizes. The subpopulation of high-density, low-mass cells visible at the later time points likely corresponds to dead cells, reaching as much as 20-30% of the total cells in culture. One reason for the relatively large numbers of dead cells is that no centrifugation

or dead cell removal steps were included between cell culture and density measurement to avoid biasing the population measurements.

The heterogeneity observed in the response to activation remains an interesting open question. Further work linking these mass, volume, and density measurements to other deep single-cell measurements such as single-cell RNA-seq could potentially provide some insight into the roles of these different cell types.

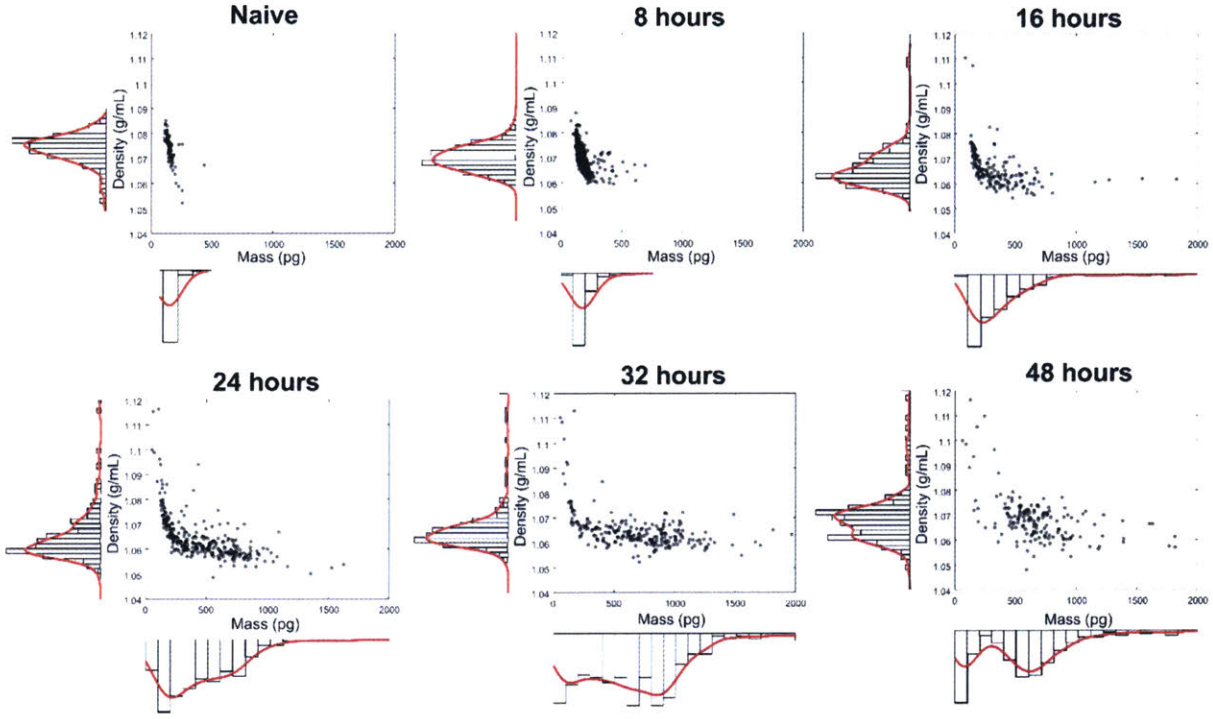

Figure 11. Dynamics of single-cell density and mass changes in the first 48 hours of T cell activation.

Interestingly, in this measurement, a larger fraction of "blasted" cells was observed at the first time point than is observed when measuring changes in the mass accumulation rates of the same cells during activation. One possible explanation is that cellular composition is altered significantly during activation, so monitoring buoyant mass accumulation alone may not accurately reflect changes in cell size. Specifically, during activation, T cells appear to increase in absolute mass but decrease in density, and since the SMR measures *buoyant* mass, an increase in absolute mass could be offset by a decrease in density. To illustrate how cells of different size can have the same buoyant mass, Fig. 12 plots contours of constant buoyant mass in cell density-cell mass space, for a medium of density 1.003 g/mL. All cells whose density and mass lie on the same

contour have the same buoyant mass, and could not be distinguished by a single buoyant mass measurement. The contours come from rearranging the definition of buoyant mass, i.e.,

$$m_{cell}\left(1-\frac{\rho_f}{\rho_{cell}}\right) = \text{constant}$$

For reference, the vertical asymptote is $m_{cell} = 0$ (i.e., a cell with zero mass will weigh nothing regardless of the fluid density), and the horizontal asymptote is $\rho_{cell} = \rho_f$ (i.e., when the cell density is equal to the fluid density, all cells will appear to have the same (zero) buoyant mass).

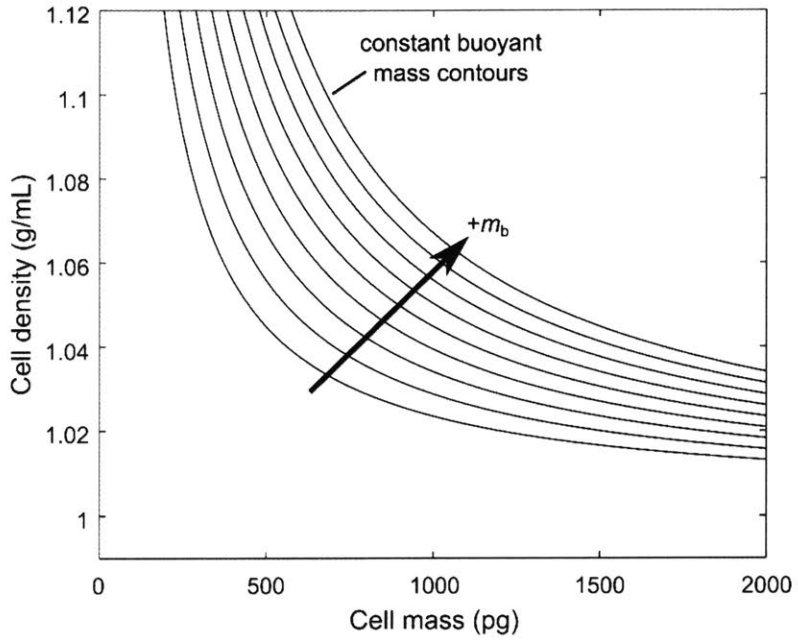

Figure 12. Contours of constant buoyant mass. Different cells whose densities and masses lie on the same contour will have the same buoyant mass when measured in the same fluid, while in reality the cells may be of very different absolute sizes.

We can also see that *buoyant mass* accumulation rate measured by the SMR differs from the *total* mass accumulation rate if a cell's density is also changing, i.e., if the volume does not change in proportion to the total mass:

$$\frac{dm_b}{dt} = \frac{d}{dt}\left(m_{cell}\left(1-\frac{\rho_{fluid}}{\rho_{cell}}\right)\right) = \left(1-\frac{\rho_{fluid}}{\rho_{cell}}\right)\frac{dm_{cell}}{dt} + \left(\frac{m_{cell}\rho_{fluid}}{\rho_{cell}^2}\right)\frac{d\rho_{cell}}{dt} \quad [4]$$

Some order-of-magnitude approximations show how mass accumulation is no longer proportional to buoyant mass accumulation when density is also changing rapidly. In the mouse $CD8^+$ T cell activation experiments, the rate of density change was of order 0.01 g/mL over 10 hours. Using

typical values for large cells (buoyant mass accumulation rate ~ 5 pg/hr, mass ~ 500 pg, density ~ 1.05 g/mL), Eq. 4 suggests that the decreasing density can cause buoyant mass accumulation measurements to underestimate the total mass accumulation rate by as much as 10-20%. This reduction could obscure rapid shifts in buoyant mass accumulation for large cells, which are still detected by measurements of *total* mass.

4.1.2 Human healthy vs. CLL CD8+ T cells

Chronic lymphocytic leukemia (CLL) is primarily thought of as a B cell disease, but T cell synapse formation and activation is suspected to be impaired as well[21]. To determine whether density measurements could discriminate between phenotypically distinct T cell populations (healthy vs. CLL), we isolated $CD8^+$ T cells from the blood of both healthy and CLL donors. The cells were activated using anti-human CD3 antibody, with co-stimulation provided by anti-human CD28. The population was sampled and density measurements were taken over 96 hours (Fig. 13). The naïve cell populations from the two donors nearly coincided in density-mass space. However, by 24 h after activation, the large subpopulation of high-density, low mass cells suggests that a significant fraction of the CLL cells had died off. By the last time point, 96 h after activation, approximately 58% of cells from the healthy donor had blasted, compared to only 34% of the cells from the CLL donor. This dataset suggests that density and mass measurements can in fact distinguish between these two phenotypically distinct T cell populations.

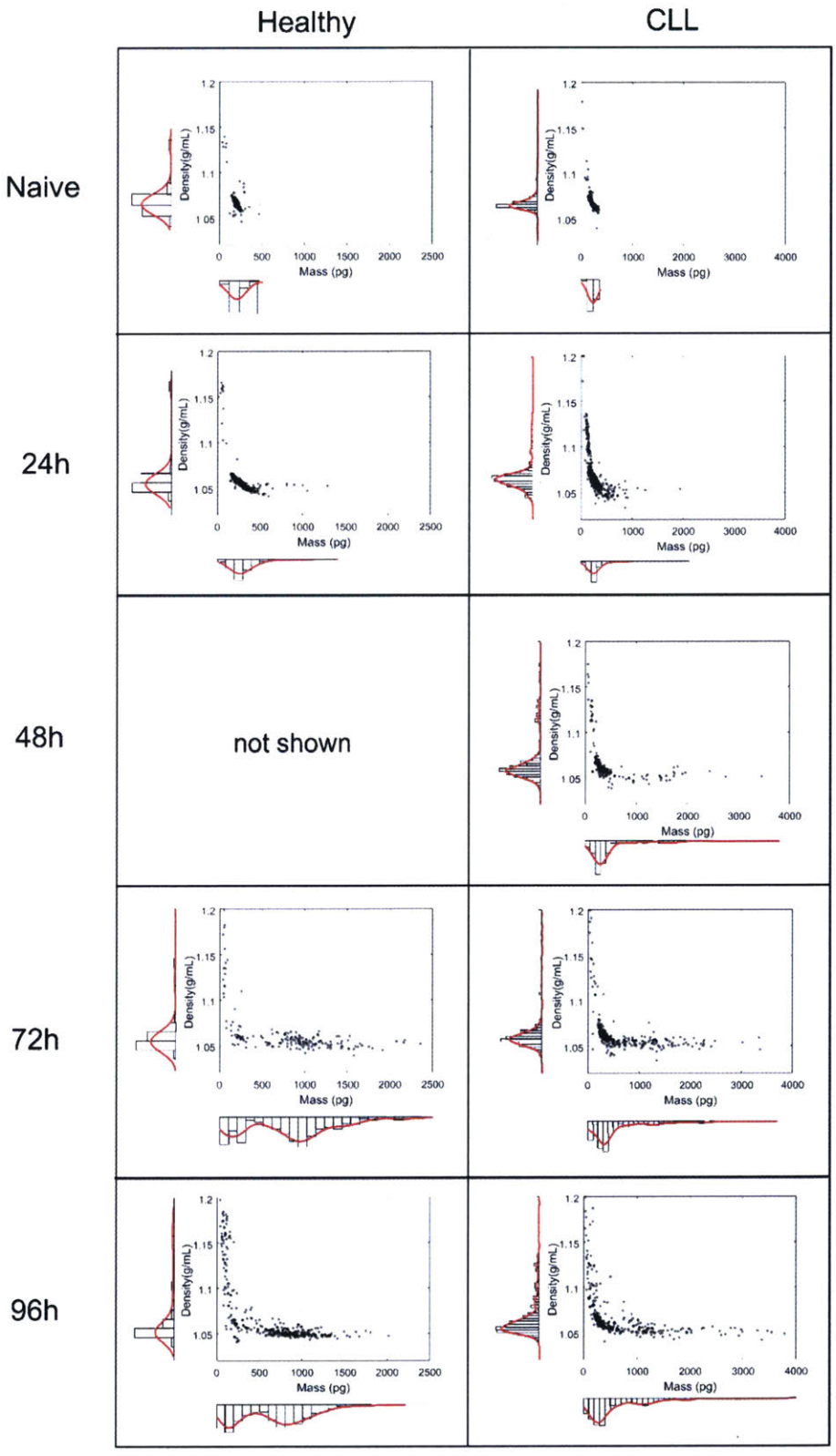

Figure 13. Mass and density of activated CD8+ T cells from healthy and CLL donors.

Chapter 5

Materials and methods

5.1 Murine CD8+ T cell isolation and activation

$CD8^+$ T cells were isolated from the spleens of wild-type mice via negative magnetic selection (Miltenyi, CD8+ T cell Isolation Kit). T cells were activated by plating them at a concentration of 2 x 10^6 cells mL^{-1} in a high-bind 96-well plate (Corning) coated with 5 μg mL^{-1} anti-mouse CD8 antibody (clone: 145-2C11, BioLegend catalog number 100314) while having 2 μg mL^{-1} anti-mouse CD28 (clone: 37.51, BioLegend catalog number 102112) and 100 U/mL mouse IL-2 (Miltenyi) in solution. The cells were cultured in RPMI medium (Thermo Fisher) supplemented with 10% heat-inactivated fetal bovine serum (FBS), 25 mM HEPES, 55 μM beta-mercaptoethanol (Gibco), and 1% antibiotic-antimycotic (Gibco). Cells were cultured for 8, 16, 24, 32, or 48 hours, then collected and resuspended in fresh medium at a concentration of approximately 30,000 cells mL^{-1} for measurement.

5.2 Human CD8+ T cell isolation and activation

Human blood buffy coated was obtained from Research Blood Components. Peripheral blood mononuclear cells (PBMCs) were isolated via density gradient centrifugation (Ficoll-Paque Plus, GE). Red blood cells were lysed (ACK buffer, Thermo Fisher) and washed with RPMI supplemented with 10% heat-inactivated fetal bovine serum (FBS). $CD8^+$ T cells were isolated via negative magnetic selection (Miltenyi $CD8^+$ T cell Isolation Kit), then seeded at a density of 2 x 10^6 cells mL^{-1} in a high-bind 96-well plate (Corning) coated with 5 μg mL^{-1} anti-human CD3 (clone HIT3a, BioLegend) while having 2 μg mL^{-1} anti-human CD28 (clone CD28.2, BioLegend) and 100 U/mL IL-2 (PeproTech) in solution. Cells were cultured in RPMI 1640 supplemented with 10% heat-inactivated FBS, 25 mM HEPES, and 1% antibiotic-antimycotic (Gibco). Cells were resuspended in fresh medium at a density of approximately 30,000 cells mL^{-1} for measurement.

5.3 Details of density measurement protocol

The bypasses leading to the first and third cantilevers were loaded with culture medium. The bypass leading to the second cantilever was loaded with 30% Optiprep/70% culture medium (density ~1.07 g/mL) to ensure isoosmolarity. The percentage of fluid exchange between cantilevers could be controlled (to some extent) by varying the relative flow rates in each bypass and across cantilever. Since the density of each solution is known, monitoring the baseline resonance frequency in each cantilever allowed calculation of the fluid density in each cantilever, and therefore the actual composition of the fluid in each cantilever. Under typical operating conditions, 60-80% fluid exchange was achieved between sensors (i.e., the second cantilever contained 60-80% of solution 2 which contained 30% Optiprep, and 20-40% of solution 1, which was just culture medium). This resulted in typical fluid densities of 1.00 g/mL, 1.04 g/mL, and 1.02 g/mL in the first, second, and third cantilevers. In a typical measurement these values varied by less than 0.001 g/mL over the course of the experiment.

For typical suspension cell measurements, cells were loaded into the first bypass channel at a concentration of 30,000 cells mL^{-1}. At an average spacing of one cell entering the array per 5-10 seconds, a typical experiment measured 300-600 cells over the course of an hour. This cell spacing was limited by the requirement to match measurements downstream rather than any physical or fluid mixing requirements. Typical transit times between cantilevers were 4-6 seconds.

Chapter 6

Conclusions and future work

Changes in cell density likely reflect the integration of many intracellular processes, but little is known about the extent to which cells sense or control their mass-to-volume ratio – largely because of limited techniques available for measuring density at the single-cell level. Future work will involve linking single-cell density measurements with downstream analysis such as scRNA-seq, to gain some insight into the observed heterogeneity in density measurements, e.g., within the early stages of T cell activation.

It would also be interesting to evaluate precise single cell volume measurements as a method of normalizing transcriptomics data. Typical metrics such as TPM (transcripts per million) or FPKM (fragments per kilobase per million mapped reads) attempt to normalize expression results for cell size by comparing the number of observed transcripts for a particular gene to the total number of observed transcripts. Others have used RNA spike-ins to estimate the absolute RNA content per cell[22]. Precise volume measurements linked with scRNA-seq data would enable direct evaluation of each of these techniques. Since most cells have approximately the same density, it is possible that a single buoyant mass measurement could be sufficient to approximate cell volume for normalization.

Appendices

Appendix 1. Notes on simultaneously measuring density and dry density

The key to measuring a cell's density using the fluid exchange approach is recognizing that the density of the intracellular contents is not affected by the fluid exchange because the cell is impermeable to the high-density fluid. The cell's aqueous content – which is neutrally buoyant in aqueous solutions – buoys up the cell in the impermeable high-density fluid, reducing the cell's buoyant mass.

Alternatively, if the cell membrane is *also* permeable to the high-density fluid, the cell's aqueous content remains neutrally buoyant after the fluid exchange; therefore, the measured buoyant mass results only from the cell's non-aqueous content. Therefore, pairing measurements of a cell's buoyant mass in two aqueous solutions of different densities (e.g., H_2O- and D_2O-based solutions) allows measurement of the mass, volume, and density of the cell's non-aqueous content, or its "dry" mass, volume, and density, as described previously[8].

The three-cantilever devices described in this thesis could conceivably be used to obtain measurements of a cell's buoyant mass in three different fluids – such as H_2O-based media, D_2O-based media, and Optiprep – in order to determine each cell's mass, volume, and density as well as its dry mass, dry volume, and dry density. Since the device as designed typically results 60-80% fluid exchange between sensors, here we consider how imperfect fluid exchange would affect the calculated density and dry density.

These calculations are somewhat tedious, but it is helpful to carefully consider how different cellular contents contribute to buoyant mass to ensure we are accurately computing derived quantities such as density and dry density from the measured buoyant masses.

Assume we measure the cell in an impermeable fluid such as Optiprep ("OP") in the first sensor, H_2O-based media ("H_2O") in the second sensor, and D_2O-based media ("D_2O") in the third sensor. First, how is the buoyant mass measured in each sensor related to the cell's physical properties (which do not change) and the fluid density in each sensor? In the first cantilever filled with 100% Optiprep (density ρ_1), the measured buoyant mass is

$$m_{b,OP} = \rho_{dry}V_{dry} + \rho_{H2O}V_{iw} - (V_{dry} + V_{iw})\rho_1$$

In which ρ_{dry} is the cell's dry density, ρ_{H2O} is the density of water, V_{dry} is the cell's dry volume, V_{iw} is the intracellular water volume. Since the cell is impermeable to the surrounding fluid, the cell is buoyed up by the mass of (relatively dense) fluid that it displaces.

The second cantilever contains a mixture of water (density ρ_{H2O}) and Optiprep (ρ_{OP}). The density of the fluid in the second cantilever depends on the relative proportions of Optiprep and water present in the mixture, described in terms of the percent fluid exchange, f_{12}, i.e., $\rho_2 = f_{12}\rho_{H2O} + (1 - f_{12})\rho_{OP}$, where perfect fluid exchange corresponds to $f_{12} = 1$. Since the cell membrane is impermeable to Optiprep, the density of the intracellular fluid is still ρ_{H2O}, and the intracellular water volume contributes to the measured buoyant mass an amount $\Delta m = (\rho_2 - \rho_{H2O})V_{iw}$. The measured buoyant mass in the second sensor is then

$$m_{b,H2O} = \rho_{dry}V_{dry} + \rho_{H2O}V_{iw} - (V_{dry} + V_{iw})\rho_2$$

The third cantilever contains primarily D_2O, with a smaller amount of H_2O and a negligible amount of Optiprep, i.e., $\rho_3 = f_{23}\rho_{D2O} + (1 - f_{23})\rho_2 \approx f_{23}\rho_{D2O} + (1 - f_{23})\rho_{H2O}$, where f_{23} is the percent fluid exchange between the second and third cantilevers. The measured buoyant mass is then related to the cell's volume and density by

$$m_{b,D2O} = \rho_{dry}V_{dry} + \rho_{iw}V_{iw} - (V_{dry} + V_{iw})\rho_3$$

Note that under the assumption of negligible Optiprep in the third cantilever, the cell's intracellular water content is approximately neutrally buoyant ($\rho_3 \approx \rho_{iw}$), and the buoyant mass simplifies to

$$m_{b,D2O} \approx (\rho_{dry} - \rho_3)V_{dry}$$

Cell density

Using these definitions, first we confirm that our calculated cell density is not affected by the fluid exchange percentage f_{12}. Cell density is defined as its mass to volume ratio, i.e.,

$$\rho_{cell} = \frac{\rho_{cell}V_{dry} + \rho_{H2O}V_{iw}}{V_{dry} + V_{iw}}$$

Rearranging the equations for buoyant masses in the first and second cantilevers, we can rewrite the measured buoyant masses in terms of the cell density:

$$m_{b,OP} = (\rho_{cell} - \rho_1)(V_{dry} + V_{iw})$$

$$m_{b,H2O} = (\rho_{cell} - \rho_2)(V_{dry} + V_{iw})$$

Dividing the two and solving for the cell density, we are left with the familiar formula

$$\rho_{cell} = \frac{m_{b,H2O}\rho_1 - m_{b,OP}\rho_2}{m_{b,H2O} - m_{b,OP}}$$

i.e., regardless of the percent fluid exchange between the first two sensors, we can compute the cell's density as long as the density in the second fluid (a mixture of Optiprep and water) is known. This confirms a known result – there is no need to attempt to exchange 100% of a cell's surrounding fluid to achieve accurate measurements of cell density.

Dry density

We now apply the same approach to show that the dry density measured using the three-cantilever device *does* depend on the fluid exchange percentage between the first and second sensors. Rearranging, the buoyant masses in the second and third cantilevers are

$$m_{b,H2O} = V_{dry}(\rho_{dry} - \rho_2) + V_{iw}(\rho_{H2O} - \rho_2) \quad [5]$$

$$m_{b,D2O} = V_{dry}(\rho_{dry} - \rho_3) \quad [6]$$

The term $V_{iw}(\rho_{H2O} - \rho_1)$ appears because the intracellular water content is not neutrally buoyant in the second cantilever due to the presence of some Optiprep in the surrounding fluid. In the limit of perfect fluid exchange between the first and second cantilevers, the second fluid is composed entirely of H_2O with no Optiprep ($f_{12} \to 1$), and the density of the second fluid is just the density of the H_2O-based medium ($\rho_2 \to \rho_{H2O}$). In this ideal limit the dry density is obtained by solving (5) and (6), resulting in

$$\rho_{dry} = \frac{m_{b,H2O}\rho_3 - m_{b,D2O}\rho_2}{m_{b,H2O} - m_{b,D2O}} \quad [7]$$

i.e., again we can compute the cell's dry density from its buoyant masses measured in H_2O-based and D_2O-based fluids regardless of the percent fluid exchange as long as we know the density of each fluid.

However, in real measurements, we don't have perfect fluid exchange and the buoyant mass measured in the second cantilever is decreased due to the presence of a small amount of Optiprep, meaning Eq. 7 no longer holds. If we aren't able to assume that $f_{12} \to 1$, an alternative approach is to attempt to "correct" the second buoyant mass measurement given the known cell density to account for the presence of trace amounts of Optiprep in the sensor, i.e., we would like to correct the buoyant mass measured in the second cantilever such that $m_{b,corr} = V_{dry}(\rho_{dry} - \rho_2)$ as in the ideal case. One way of doing so is as follows:

$$m_{b,corr} = V_{dry}(\rho_{dry} - \rho_2) = m_{b,H2O} + V_{iw}(\rho_2 - \rho_{H2O}) = m_{b,H2O} + \Delta m$$

i.e., we account for the negative (floating) buoyant mass of the intracellular water volume in the second cantilever, to estimate what the buoyant mass *would be* if the cell were being measured in 100% H_2O. The measured H_2O buoyant mass is corrected by an amount $\Delta m = (\rho_2 - \rho_{H2O})V_{iw}$. However, the intracellular water volume is not yet known since we have yet to compute the dry density. Instead, we can write another equation involving V_{iw}: from the definition of buoyant mass,

$$V_{dry} + V_{iw} = \frac{m_{b,H2O} - m_{b,OP}}{\rho_1 - \rho_2}$$

However, this introduces another variable, V_{dry} which is still unknown. We can write one more equation involving V_{dry} and the intracellular fluid buoyant mass Δm:

$$V_{dry} = \frac{(m_{b,H2O} - \Delta m) - m_{b,D2O}}{\rho_3 - \rho_2}$$

To summarize, to accurately compute a cell's dry density when its buoyant mass in water was measured in the presence of some Optiprep (or another impermeable fluid), we can solve the following three equations for V_{dry}, V_{iw}, and Δm:

$$\Delta m = (\rho_2 - \rho_{H2O})V_{iw}$$

$$V_{dry} + V_{iw} = \frac{m_{b,H2O} - m_{b,OP}}{\rho_1 - \rho_2}$$

$$V_{dry} = \frac{(m_{b,H2O} - \Delta m) - m_{b,D2O}}{\rho_3 - \rho_2}$$

Then use the "corrected" buoyant mass to compute the dry density according to

$$\rho_{dry} = \frac{(m_{b,H2O} + \Delta m)\rho_3 - m_{b,D2O}\rho_2}{(m_{b,H2O} + \Delta m) - m_{b,D2O}}$$

Fig. 14 illustrates this approach; the buoyant mass measurement in water is adjusted to correct the dry density estimate.

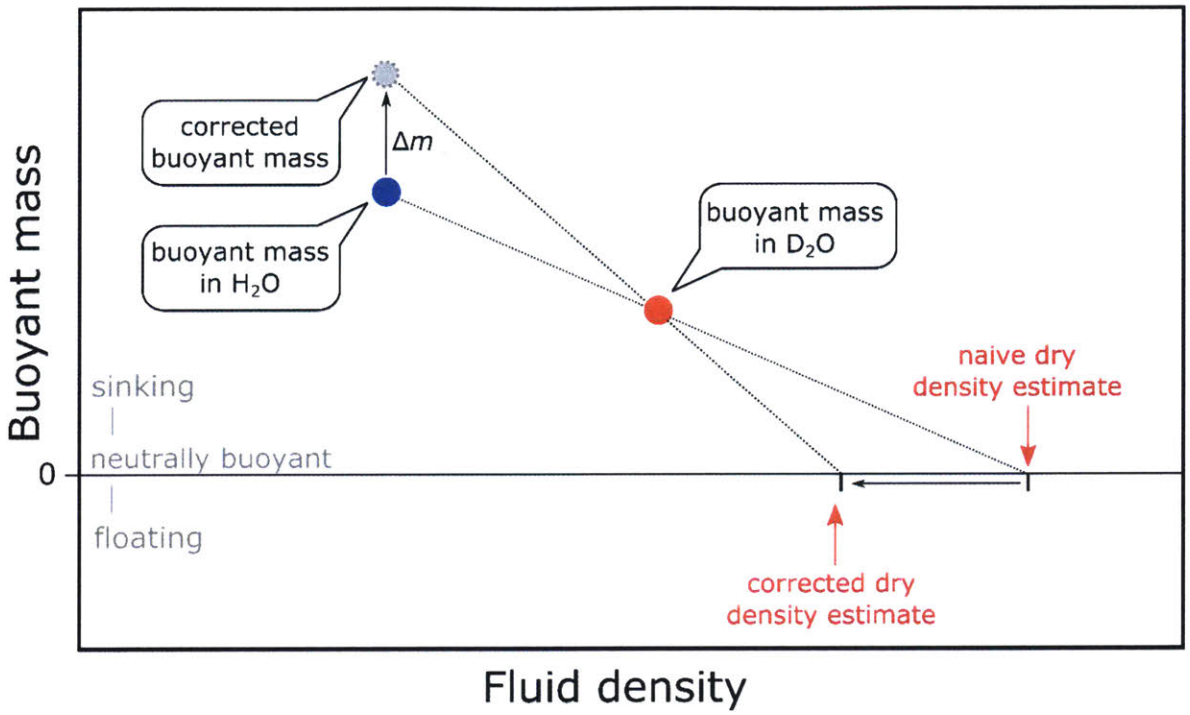

Figure 14. Dry density can be potentially be estimated when a cell is weighed in three fluids by correcting the measured buoyant mass in water to account for the presence of trace amounts of Optiprep.

Appendix 2. General approach to controlling flow through microfluidic network

A three-step process makes it straightforward to compute the pressures required to independently control the flow rates through each edge of a fluidic network. This model neglects channel compliance, and so it is most suited for describing flow through rigid microfluidic devices (such as silicon) rather than softer ones (such as PDMS).

As an example, consider the fluidic network shown in Fig. 15. The network consists of nine branches and ten nodes (intersections of branches, which are nominally at the same pressure). The goal is to produce the desired flow rates $Q_1 \ldots Q_5$ by controlling the pressures $p_1 \ldots p_5$. (The flow rates across any five edges could be specified as long as they are self-consistent, i.e., satisfy mass conservation).

The pressures at the external nodes are controllable (connected to pressure regulators), while the pressures at the internal nodes are not directly controlled. Resistance estimates (R_1, R_2, R_3) come from the standard Poiseuille flow model, i.e., $R = 128\mu L/\pi {D_h}^4$, where L is the length of the branch and D_h is the hydraulic diameter.

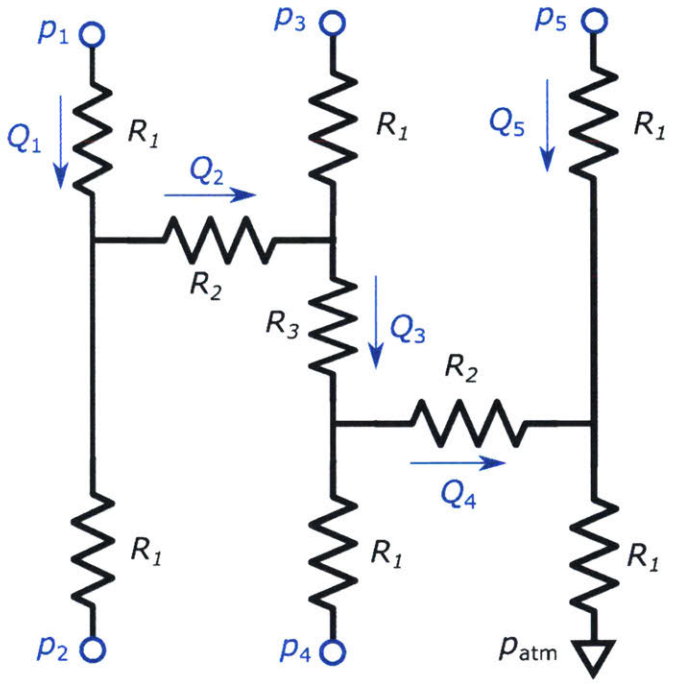

Figure 15. Fluidic network used to demonstrate pressure calculations. The objective is to produce the desired flow rates $Q_1 \ldots Q_5$ by controlling the pressures $p_1 \ldots p_5$.

First, we compute the pressures at the internal (uncontrolled) nodes using by writing constraint equations enforcing mass conservation at each node. By setting the sum of the flows into each internal node equal to the sum of flows out of each node, we can write one equation per node. In matrix form, these equations are:

$$AP_i = \begin{pmatrix} \frac{1}{R_1}+\frac{1}{R_1}+\frac{1}{R_2} & -\frac{1}{R_2} & 0 & 0 \\ -\frac{1}{R_2} & \frac{1}{R_1}+\frac{1}{R_2}+\frac{1}{R_3} & -\frac{1}{R_3} & 0 \\ 0 & -\frac{1}{R_3} & \frac{1}{R_1}+\frac{1}{R_2}+\frac{1}{R_3} & -\frac{1}{R_2} \\ 0 & 0 & -\frac{1}{R_2} & \frac{1}{R_1}+\frac{1}{R_1}+\frac{1}{R_2} \end{pmatrix} \begin{pmatrix} p_a \\ p_b \\ p_c \\ p_d \end{pmatrix}$$

$$= \begin{pmatrix} \frac{1}{R_1} & \frac{1}{R_1} & 0 & 0 & 0 \\ 0 & 0 & \frac{1}{R_1} & 0 & 0 \\ 0 & 0 & 0 & \frac{1}{R_1} & 0 \\ 0 & 0 & 0 & 0 & \frac{1}{R_1} \end{pmatrix} \begin{pmatrix} p_1 \\ p_2 \\ p_3 \\ p_4 \\ p_5 \end{pmatrix} = BP$$

If the geometry we have specified is self-consistent, A is invertible and the pressures at the internal nodes are given by $P_i = A^{-1}BP$. Next, concatenate P and P_i to write the pressure "state" vector containing the pressure at *all* nodes, i.e. (in block matrix format)

$$\begin{pmatrix} p_1 \\ p_2 \\ p_3 \\ p_4 \\ p_5 \\ p_a \\ p_b \\ p_c \\ p_d \end{pmatrix} = \begin{pmatrix} I_{5x5} \\ A^{-1}B \end{pmatrix} \begin{pmatrix} p_1 \\ p_2 \\ p_3 \\ p_4 \\ p_5 \end{pmatrix} = MP$$

This pressure state vector contains both the controlled and uncontrolled pressures, making it easy to specify the desired flow rate across any five branches of the network. For example, to specify $Q_1 \ldots Q_5$ across the branches labeled with arrows in Fig. 15, we can write

$$Q = \begin{pmatrix} Q_1 \\ Q_2 \\ Q_3 \\ Q_4 \\ Q_5 \end{pmatrix} = \begin{pmatrix} \frac{1}{R_1} & 0 & 0 & 0 & 0 & -\frac{1}{R_1} & 0 & 0 & 0 \\ 0 & 0 & 0 & 0 & 0 & \frac{1}{R_2} & -\frac{1}{R_2} & 0 & 0 \\ 0 & 0 & 0 & 0 & 0 & 0 & \frac{1}{R_3} & -\frac{1}{R_3} & 0 \\ 0 & 0 & 0 & 0 & 0 & 0 & 0 & \frac{1}{R_2} & -\frac{1}{R_2} \\ 0 & 0 & 0 & 0 & \frac{1}{r} & 0 & 0 & 0 & -\frac{1}{R_1} \end{pmatrix} \begin{pmatrix} p_1 \\ p_2 \\ p_3 \\ p_4 \\ p_5 \\ p_a \\ p_b \\ p_c \\ p_d \end{pmatrix} = C \begin{pmatrix} p_1 \\ p_2 \\ p_3 \\ p_4 \\ p_5 \\ p_a \\ p_b \\ p_c \\ p_d \end{pmatrix} = CMP$$

Finally, we can implement these desired flow rates by setting the controlled pressures $p_1 \ldots p_5$ to the values given by $P = (CM)^{-1}Q$.

References

1. W.H. Grover, A.K. Bryan, M. Diez-Silva, S. Suresh, J.M. Higgins, S.R. Manalis. *Proc. Natl. Acad. Sci. U. S. A.*, 2011, **108**, 10992–6.
2. P.K. Raghuprasad. *J. Imm*, 1982, **129**, 2128–33.
3. A. Zipursky, E. Bow, R. Seshadri, E. Brown. *Blood*, 1976, **48**, .
4. A.K. Bryan, V.C. Hecht, W. Shen, K. Payer, W.H. Grover, S.R. Manalis. *Lab Chip*, 2014, **14**, 569–76.
5. M. Godin, A.K. Bryan, T.P. Burg, K. Babcock. 2007, 17–9.
6. S. Son, J.H. Kang, S. Oh, M.W. Kirschner, T.J. Mitchison, S. Manalis. 2015, **211**, 757–63.
7. V.C. Hecht, L.B. Sullivan, R.J. Kimmerling, D.H. Kim, A.M. Hosios, M.A. Stockslager, et al. 2016, **212**, 439–47.
8. F. Feijó Delgado, N. Cermak, V.C. Hecht, S. Son, Y. Li, S.M. Knudsen, et al. *PLoS One*, 2013, **8**, e67590.
9. R. Barer, S. Joseph. *J. Cell Sci.*, 1954, **95**, 399–423.
10. T.P. Burg, M. Godin, S.M. Knudsen, W. Shen, G. Carlson, J.S. Foster, et al. *Nature*, 2007, **446**, 1066–9.
11. T.P. Burg, S.R. Manalis. *Appl. Phys. Lett.*, 2003, **83**, 2698–700.
12. S. Olcum, N. Cermak, S.C. Wasserman, S.R. Manalis. *Nat. Commun.*, 2015, **6**, 1–8. Available from: http://dx.doi.org/10.1038/ncomms8070
13. Y. Weng, F. Feij, S. Son, T.P. Burg, C. Wasserman, S.R. Manalis. 2011, 4174–80.
14. A.K. Bryan. 2011, .
15. N. Cermak, S. Olcum, F.F. Delgado, S.C. Wasserman, K.R. Payer, M.A. Murakami, et al. 2016, **34**, .
16. Y. Cao. MATLAB File Exchange. 2011.
17. D.C. Montgomery, G.C. Runger. 2011.
18. W.M. Deen. 1998.
19. W.J. Pichler, J. Tilch. 2004, 809–20.
20. R.M. Bohmer, E. Bandala-Sanchez, L.C. Harrison. 2011, .
21. A.G. Ramsay, A.J. Johnson, A.M. Lee, G. Gorgün, R. Le Dieu, W. Blum, et al. 2008, **118**, 2427–37.

22. G.K. Marinov, B.A. Williams, K. Mccue, G.P. Schroth, J. Gertz, R.M. Myers, et al. 2014, 496–510.